Journal of Physics: Photonics

CrossMark

OPEN ACCESS

RECEIVED
21 October 2020

REVISED
7 December 2020

ACCEPTED FOR PUBLICATION
10 January 2021

PUBLISHED
3 February 2021

PAPER

Nanoscale investigation of two-photon polymerized microstructures with tip-enhanced Raman spectroscopy

Anastasiya V Kazantseva[1], **Elena A Chernykh**[1], **Cameron Crook**[2], **Evan P Garcia**[2], **Dmitry A Fishman**[3], **Eric O Potma**[3], **Lorenzo Valdevit**[2], **Sergey S Kharintsev**[1,4] **and Tommaso Baldacchini**[3]

[1] Department of Optics and Nanophotonics, Institute of Physics, Kazan Federal University, Kazan 420008, Russia
[2] Materials Science and Engineering Department, University of California, Irvine, CA 92697, United States of America
[3] Department of Chemistry, University of California, Irvine, CA 92697, United States of America
[4] Institute of Applied Research, Tatarstan Academy of Science, Kazan 420111, Russia

E-mail: skharint@gmail.com **and** tbaldacchini@gmail.com

Keywords: 3D nano-printing, two-photon polymerization, Raman spectroscopy, near-field enhancement

Abstract

We demonstrate the use of tip-enhanced Raman spectroscopy (TERS) on polymeric microstructures fabricated by two-photon polymerization direct laser writing (TPP-DLW). Compared to the signal intensity obtained in confocal Raman microscopy, a linear enhancement of almost two times is measured when using TERS. Because the probing volume is much smaller in TERS than in confocal Raman microscopy, the effective signal enhancement is estimated to be ca. 10^4. We obtain chemical maps of TPP microstructures using TERS with relatively short acquisition times and with high spatial resolution as defined by the metallic tip apex radius of curvature. We take advantage of this high resolution to study the homogeneity of the polymer network in TPP microstructures printed in an acrylic-based resin. We find that the polymer degree of conversion varies by about 30% within a distance of only 100 nm. The combination of high resolution topographical and chemical data delivered by TERS provides an effective analytical tool for studying TPP-DLW materials in a non-destructive way.

1. Introduction

Two-photon polymerization direct laser writing (TPP-DLW) was first used to produce a three-dimensional microstructure in 1997, and since then this additive manufacturing technique has matured into an enabling technology for a vast number of research fields [1]. Presently, TPP-DLW is routinely used to print one-of-a-kind parts that are employed in applications ranging from micro-optics to tissue engineering, from mechanical and photonics metamaterials to microfluidics [2, 3]. Furthermore, with the advent of 4D printing, TPP-DLW has the potential to play a fundamental role in micro- and nano-robotics with far-reaching applications in biology and medical devices [4].

TPP-DLW enables the confinement of matter transformation (liquid to solid in the case of negative-tone resins) within volume elements (voxels) that, depending on the employed focusing optics and excitation wavelengths, reach values as small as sub-femtoliters [5]. As a result, TPP-DLW is a true free-form manufacturing process capable of printing three-dimensional microstructures with no restrictions on their architectural design, yet with remarkable accuracy. These characteristics, in combination with a relatively wide assortment of available materials and a variety of post-processing procedures that permit transformation of polymeric frameworks into semiconductor, conductor, and ceramic components, are unquestionably the reasons of the success of TPP-DLW in so many research areas [6].

Two aspects of TPP-DLW that have received considerable attention since its inception are the minimum achievable feature size and the maximum writing resolution. While research in the former aspect has produced astounding results almost immediately, research in the latter aspect has seen a slower development and the concomitant efforts from several groups to deliver positive outcomes [7].

To understand the ability of TPP-DLW to produce small feature sizes, the laser intensity threshold (I_{th}) needs to be taken into consideration, and the fact that, below this threshold, photopolymerizable resins are not sufficiently cross-linked. From a practical point of view, this means that objects created by TPP-DLW need to be fabricated using laser intensities higher than I_{th} if they are to survive the development step. Hence, polymerized features with smaller and smaller dimensions can be printed by TPP-DLW using ever decreasing laser intensities that barely surpass I_{th}. In this way, the volume of the laser-focused beam is not polymerized in its entirety but only in those regions where the intensity surpasses the threshold. Using this strategy, nanorods as thin as 30 nm have been written using an excitation wavelength of 800 nm [8].

While the optical diffraction limit can be broken in TPP-DLW when printing single and well-separated elements (i.e. voxels or continuous lines), the writing resolution (inter-elements distance at which elements are still distinguishable) suffers from limiting mechanisms that are inherent to the polymerization process. Specifically, due to the so-called memory effect of the resin, the minimum achievable distance between two voxels or lines in TPP-DLW is always two to five times larger than the minimum feature size. As a consequence, the highest writing resolution reported so far when using TPP-DLW in its original form is around 200 nm [9]. Over the years, several research groups have developed clever strategies to overcome this limitation [10–14]. Many of these strategies were inspired by the astounding results achieved in fluorescent-based super-resolution microscopy techniques such as STED and RESOLFT [15].

Based on the above discussion then, it is evident that TPP-DLW can reproduce three-dimensional objects at the microscale level with unmatched fidelity. Both the building blocks used to print these parts (voxels) and the proximity with which they can be positioned have indeed reached dimensions smaller than 100 nm. Unfortunately, the ability to control matter transformation with such a high spatial accuracy has not been matched by the implementation of adequate analytical techniques that can investigate the polymerization process at the same or smaller length scales. For example, confocal Raman microscopy is often used to characterize TPP microstructures because of its ability to retrieve chemical-rich information [16]. Since it is a far-field (FF) optical technique, Raman microscopy is limited in its spatial resolution by the diffraction limit. Thus, discriminating signals from sample domains that are separated by less than 300 nm is extremely challenging using this technique.

Therefore, we believe that the decisive advance of TPP-DLW into a widely used micro- and nano-manufacturing process calls for an analytical technique capable of characterizing structures at sub-diffraction limited spatial resolution. Working towards this goal, we demonstrate the use of near-field (NF) microscopy to investigate the chemical properties of TPP microstructures with a resolution well below 100 nm. Specifically, we collect Raman maps of TPP microstructures using tip-enhanced Raman spectroscopy (TERS) [17–19].

TERS combines the benefits of Raman spectroscopy with the spatial resolution of scanning probe microscopy. In particular, TERS produces data that is highly specific in chemical information along with signal localization down to the tens of nanometers. Accordingly, TERS has the potential to deliver label-free chemical imaging of TPP microstructures even when they are printed with the finest feature sizes and the highest writing resolution. Furthermore, the non-destructive and minimally invasive characters of TERS render this technique attractive for real-time imaging of TPP-DLW at the nanoscale.

Through the years, TERS has been utilized to study many types of nanostructured materials. Examples include single-walled carbon nanotubes, graphene flakes, organic and semiconductor solar cells, and metals-based catalysts [20–24]. TERS has been employed successfully in the characterization of biological materials as well. Bacteria, viruses, erythrocytes, and nucleic acids have all been analyzed with nano-scale resolution using TERS [25–28]. Furthermore, polymers have been the subject of TERS studies as well. In one example, a polystyrene/polyisoprene thin film was imaged by TERS resulting in new information on the surface and sub-surface nano-structure of these composite materials [29]. In another example, a different polymer blend thin film was investigated by TERS [30]. In this case, the development of the interface between the two polymers that constitute the film was followed with a high spatial resolution by imaging samples annealed at different temperatures.

Herein, we provide Raman maps of polymeric microstructures fabricated by TPP-DLW with a spatial resolution that exceeds that of conventional confocal Raman microscopy. Based on our TERS measurements, we reveal preliminary information on the nanostructure composition of printed polymeric parts. We find a conspicuous amount of heterogeneity in the polymer cross-linking along distances smaller than the size of the used polymerized voxel. This study proves that TERS can be applied to investigate TPP microstructures, paving the way to better understand photopolymerization processes when they are confined within small volumes such as in TPP-DLW.

2. Experimental methods

TPP samples were printed using a commercial TPP-DLW system (Photonic Professional GT, Nanoscribe GmbH). The excitation source is provided by a fiber-based oscillator with a center wavelength of 780 nm. The laser delivers a train of 120 fs pulses with a repetition rate of 80 MHz. The laser is focused onto the sample using a Plan-Apochromat 63 × 1.4 NA oil immersion microscope objective mounted in an inverted microscope frame. DLW is accomplished by either moving the sample with the aid of a three-axis piezo stage or by scanning the focused laser beam using galvanometric mirrors. A Bragg cell is used to regulate the laser intensity that reaches the sample and to ensure minimum amounts of over- and under-exposures. The maximum average laser power measured at the objective back aperture was 50 mW. Because of the laser wavelength and beam waist, transmission of 65% for the microscope objective was measured. All laser average powers cited hereafter refer to values measured before the microscope objective.

TPP samples were made using IP-L 780 (Nanoscribe, GmbH). IP-L 780 is a negative-tone resin that allows fast and efficient printing of three-dimensional structures by TPP-DLW. Its main component is a multifunctional acrylate monomer (pentaerythritol triacrylate, PETA) and, to start polymerization, it uses a type I photoinitiator [31]. We have chosen this resin because it enables fabrication of sub-100 nm feature sizes and because it has been well-characterized by Raman spectroscopy. Structures were fabricated on fused silica substrates modified with an adhesion promoter. After DLW, samples were submerged in propylene glycol monomethyl ether acetate for 20 min to dissolve uncured resin, followed by a 5 min long isopropanol bath for further cleaning.

FF and NF Raman spectra and mappings were captured with a multi-purpose analytical instrument NTEGRA SPECTRA™ (NT-MDT Spectrum Instruments) in the upright configuration. As it will be explained in the discussion section, an epi-collection scheme was selected for this study. The system is essentially a laser-scanning Raman confocal microscope equipped with a scanning probe station. Excitation and signal detection were carried out using a 100 × 0.7 NA microscope objective with a working distance of 6 mm.

The spectrometer was calibrated with a silicon wafer by registering a first-order Raman band centered at 520 cm^{-1}. The sensitivity of the spectrometer was ca. 2500 photon counts per 0.1 s provided that we used an exit slit of 100 μm and linearly polarized light with a center wavelength at 532 nm and an intensity of 1.5 MW cm^{-2}. The spectrometer is equipped with an EMCCD camera (ANDOR, Ireland), and it was operated at 193.15 K without signal amplification. FF and NF Raman spectra within the range of 200–2000 cm^{-1} were registered with a spectral resolution of 1.3 cm^{-1} using a 600 grooves mm^{-1} grating.

A bent gold tip attached to a tuning fork is used in the scanning probe station. The tip performs quasi vertical oscillations at the distance of 2–3 nm above the sample using feedback that is driven by a shear-force mechanism. Alignment between the apex of the gold tip with the focus of the excitation beam was realized by imaging the surface localized plasmon based field enhancement beneath the apex gold tip [32]. When turning the linear polarization direction of the excitation beam, the characteristic rotation of a two-lobe Rayleigh scattering pattern was observed at the focal plane. Following this procedure, the relative positions of the laser focus and the metallic tip were locked. TERS maps are then recorded by scanning the sample around the fixed laser focus/tip assembly by means of piezo stages and collecting Raman spectra at each pixel. Specifically, the TERS images in this work were constructed using raster scans with a step size of 5 nm and an exposure time of 0.1 s $pixel^{-1}$ resulting in 128 × 128 pixel images.

Gold tips for TERS measurements were fabricated from a 100 μm gold wire (purity: 99.99%, Goodfellow) immersed in a mixture of fuming hydrochloric acid (HCl, 37%) and ethanol [C_2H_5OH, 96%] in a 1:1 volume proportion [33, 34]. Consistent results were achieved using an adaptive dc-pulsed electrochemical etching procedure with a self-tunable duty cycle and working potentials of $V_b = 1.5$ V and $V_{up} = 1.9$ V. On achieving the current cutoff event, the tips were safely retracted from the solution surface with a piezo-manipulator and were immediately rinsed with distilled water and dried under nitrogen. Curvature radii of the gold tips were within the range of 20–30 nm. Straight and etched gold tips were first bent under mechanical load and then glued to a conductive long tab of a horizontally oriented tuning fork (TF103-NTF, NT-MDT) operating at a resonance frequency of 32 kHz. Approaching the gold tip to the sample was safely performed with the help of a normal force feedback scheme at a setpoint value as small as 95% [35].

When replacing the resonant tuning fork of the scanning probe station with a traditional silicon-based cantilever, high-resolution topographic imaging of TPP microstructures were recorded by atomic force microscopy (AFM) using tapping mode operation.

3. Results and discussions

From an experimental point of view, TERS can be implemented in a variety of excitation and detection geometries. Depending on the nature of the sample, either a bottom, side, or top illumination configurations is chosen [18]. In the latter configuration, a bent or tilted tip is often used to eliminate the possibility of shadow effects originating from the cantilever. The bottom illumination geometry requires that the Raman signal be collected using the same microscope objective used for excitation in a backscattering arrangement. Instead, the side and top illuminations can be utilized in either reflection or transmission mode.

The bottom illumination is an excellent modality for TERS measurements because it allows the use of microscope objectives with higher numerical apertures ($\geqslant$1.3). Using such objectives, the sample can be excited through evanescent waves using objective-based total internal reflection. Hence, unwanted background signal from the transmitted light does not reach the detector. Furthermore, because the evanescent wave extends over a short distance ($\sim$100 nm), only the apex of the metallic tip is illuminated. As a consequence, the bottom illumination is the most common configuration for TERS measurements, especially in demanding applications such as single-molecule studies. Unfortunately, when applied to the investigation of TPP microstructures, the bottom illumination geometry presents two drawbacks that render its implementation less than ideal. The first drawback is the short working distance of the high NA microscope objective, limiting its application to the study of thin, two-dimensional, samples. The second drawback is that transparent substrates must be used, thus excluding the use of opaque substrates. Since many applications of TPP require the manufacturing of three-dimensional patterns on silicon wafers, the bottom illumination is not a practical solution for our study. Instead, we have chosen to implement a top illumination configuration in combination with a tilted tip. This experimental configuration is quite versatile, granting the possibility to use microscope objectives with long working distances and to use substrates other than glasses. Hence, it offers ideal conditions for the investigation of TPP microstructures through TERS.

As the first experimental attempt to use TERS in the investigation of TPP-DLW, this study addresses two questions that are important for planning and executing future works. The first question concerns the amount of signal enhancement that is achievable with the experimental setup described in the previous section. Although enhancement factors (EFs) as large as 10^7 have been reported in the case of TERS of single molecules [17], these measurements are performed in high vacuum chambers using scanning tunneling microscopy probes. Hence, they are not representative of the case we are investigating. More commonly, EFs vary between 10^3 and 10^6. The second question concerns the system's ability to spatially resolve Raman signals. To realize the full potential of TERS, the spatial resolution needs to be several times higher than the one achieved by using confocal Raman microscopy.

3.1. Sample characterization

The dimensions, surface quality, and Raman signatures of the TPP sample used in our TERS studies are shown in figures 1 and 2. The microstructure consists of a rectangular pad 33 μm long and 20 μm wide printed by raster scanning using the galvanometric mirrors one layer inside the photosensitive resin with a hatching distance (hd) of 50 nm, a scan speed of 5000 μm s^{-1}, and a laser average power of 12.5 mW. Under these conditions, the radial dimension of the printed voxel is at least two times hd. Therefore, we expect the pad to result in a relatively smooth surface. Five horizontal lines 20 μm long and separated by a distance of 7 μm were then written onto the polymeric pad, this time using the piezo stages at a velocity of 30 μm s^{-1} at an average laser power of 16 mW. Although the pad and the lines were fabricated at the same axial position in the sample (the interface between the glass substrate and the resin), it can be seen from the SEM image (figure 1) that the two structures resulted in features with different thicknesses. This is better seen in the AFM image of the same microstructure (figure 2), where it is observed that the line has a thickness that is almost double the thickness of the pad. Specifically, as measured by the height plot in figure 3, the pad and the lines are 500 nm and 850 nm thick, respectively.

Printed voxels in TPP-DLW display an ellipsoidal shape because they are essentially a replica of the light intensity distribution in the focal volume. Hence, their dimensions (both axially and radially) depend on the exposure dose. The differences in thickness between the pad and the lines are easily explained by considering the larger exposure dose of the lines compared to the pad. Furthermore, the topological map of the TPP microstructure revealed that while the surface roughness of the polymeric pad is 15 nm, the surface roughness of the polymeric line is almost double that value. This is a result of the fabrication process used to make the pad, where the relatively high overlap (hd) between laser passes in the raster scan ensured sufficient polymerization in the spaces between the laser passes resulting in an overall smoother surface.

Acrylic-based resins have two characteristic Raman peaks that are used to gather information about the extent of polymerization [36]. One peak is assigned to the stretching mode of the carbon–carbon double bond and is centered at 1630 cm^{-1}. The other peak is assigned to the stretching mode of the carbon–oxygen

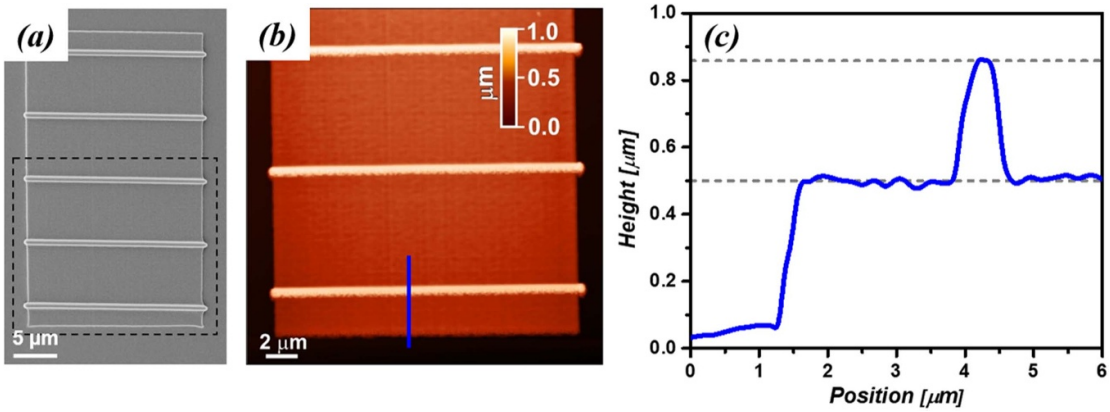

Figure 1. Dimensional and surface characterization of the TPP microstructure. (a) Top view SEM, (b) AFM of a portion of the microstructure as delineated by the square outline in (a), and (c) height profile of the sample across the blue line in (b).

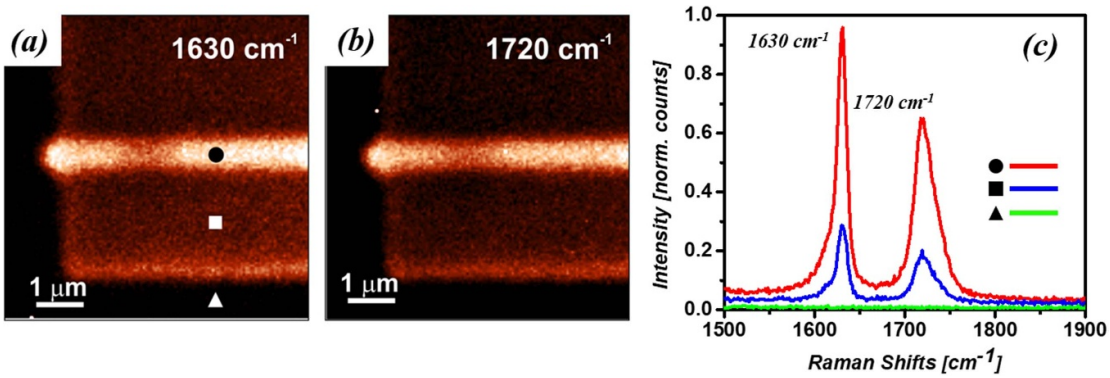

Figure 2. FF Raman characterization of the TPP microstructure. A portion of the structure shown in figure 1 is investigated using confocal Raman microscopy. Raman maps recorded using the signals at 1630 cm^{-1} and 1720 cm^{-1} are shown in (a) and (b), respectively. Raman spectra between 1500 cm^{-1} and 1900 cm^{-1} for three different locations within the sample (three points highlighted in (a) with a dot, a square, and a triangle) are shown in (c).

double bond centered at 1720 cm^{-1}. Since both the olefine and the carbonyl functional groups are intrinsic moieties of acrylic monomers, their corresponding Raman peaks are helpful spectroscopic markers for studying TPP-DLW. Specifically, while the peak at shorter wavenumber decreases upon laser irradiation because carbon–carbon double bonds are consumed during polymerization, the peak at longer wavenumbers remains essentially identical upon laser irradiation because the carbonyl group does not participate in the polymerization process. Thus, the Raman signal at 1720 cm^{-1} serves as an internal standard, and the integrated areas of these two peaks ($A_{C=C}$ and $A_{C=O}$) are used to calculate the polymerization degree of conversion (DC). DC is an important characteristic for polymers in general, but it plays an even greater role in the characterization of TPP-DLW where highly branched monomers make up most of the resins. DC values are indeed strictly correlated with several properties of TPP microstructures such as their strength and index of refraction, both of which play fundamental roles in several cutting-edge applications of TPP-DLW [37, 38].

A small area ($7 \times 7\ \mu m^2$) of the microstructure in figure 1 (bottom left) was examined using confocal Raman microscopy. Raman maps of this sample region of the sample are shown in figure 2. The signals used to build the images in figures 2(a) and (b) originate from the 1630 cm^{-1} and the 1720 cm^{-1} peaks, respectively. The two maps are almost identical with the only difference being an overall brighter signal in figure 2(a) than in figure 2(b). This difference emerges from the relative intensities of the two Raman peaks. The fact that the Raman maps in figure 2 do not display any significant differences is justified considering that the two functional groups giving rise to the measured signals are distributed within the polymer at an intra-molecular level, hence making their dispersion impossible to resolve.

Raman spectra recorded at three different locations within the sample (circle, square, and triangle points in figure 2(a)) are displayed in figure 2(c). The characteristics peaks at 1630 cm^{-1} and 1720 cm^{-1} are present in both spectra of the line and of the pad. As expected, no polymer Raman signal is measured outside the sample. Since the line's thickness is almost double that of the pad, the overall spectral intensity originating

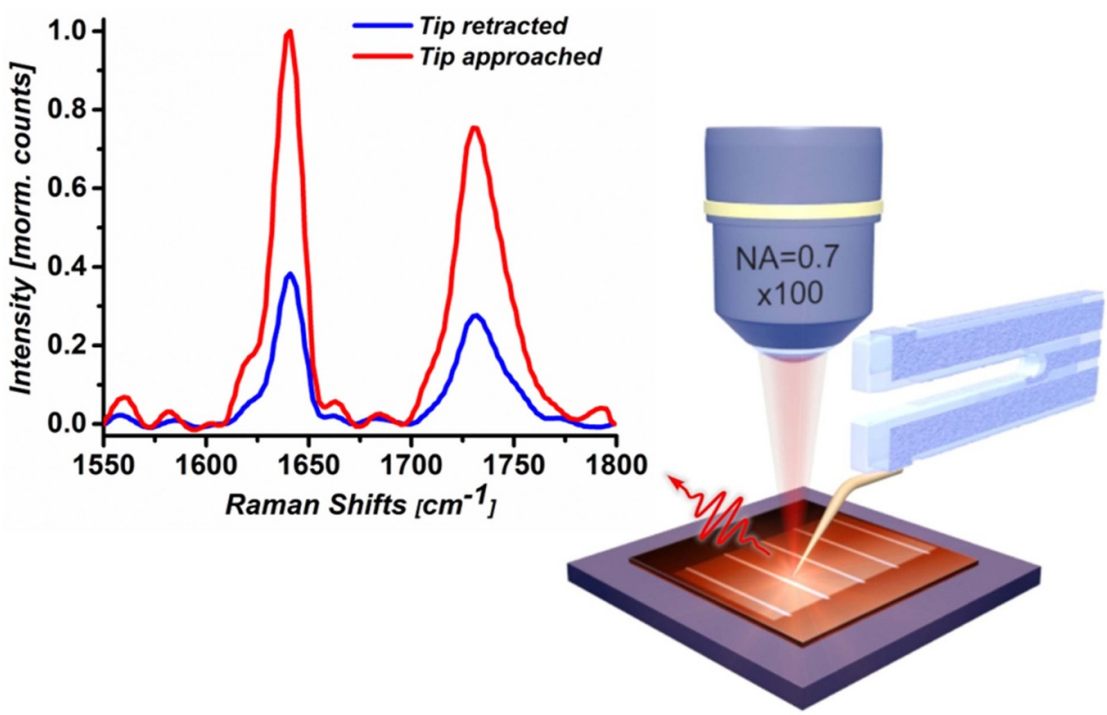

Figure 3. TERS measurement: Raman signals collected with the metallic tip either close to the sample (tip approached, red line) or far from the sample (tip retraced, blue line). The sample employed in this measurement is the same one described in figures 1 and 2. The two spectra (NF and FF) were collected from the same area of the sample, specifically the flatter part of it. A schematic of some of the elements used in the measurement is also depicted.

from the latter is significantly smaller than the one originating from the former. Nonetheless, the relative intensities of the 1630 cm^{-1} and 1720 cm^{-1} peaks are different in these two locations. They indeed give rise to DCs of 46% and 31% for the line and the pad, respectively. The larger exposure dose used to print the line not only causes a larger volume of the resin to polymerize but also a larger density of covalent bonds to be formed between the alkene functional groups of the monomers.

3.2. Signal enhancement

After this comprehensive topographical and spectroscopical characterization, we switched our experiments from FF to NF observations. Specifically, we examined the sample in figure 1(a) using TERS. A critical aspect to address when performing TERS is the measurement of the EF [17]. Knowledge of this number has relevant consequences since its value determines the experimental conditions that can be used when collecting TERS maps.

EFs in TERS are determined by making two distinct and consecutive measurements. In the first measurement, the metallic tip is moved close to the sample at a distance of a few nanometers. With the tip in this position, the Raman signal is collected. The measured signal, in this case, includes both the NF and FF Raman contributions. The NF signal originates from a minuscule volume of the sample as the result of the local field created at the metallic tip's apex. In the second measurement, the metallic tip is retracted from the sample and positioned several hundred nanometers above it. The Raman signal is then collected from the same area of the sample where the first measurement was performed. In this other case, the only contribution to the signal originates from the FF scattering of the focused laser beam in the sample. An example of these measurements is shown in figure 3 where the laser focus and metallic tip were aligned on a spot in the flatter region (pad) of the polymeric microstructure. The spectra were recorded using a laser average power of 5.4 mW and an exposure time of 30 s.

The linear enhancement is calculated by the ratio of $\left(I_{\mathrm{Tip-in}} - I_{\mathrm{Tip-out}}\right)/I_{\mathrm{Tip-out}}$, where $I_{\mathrm{Tip-in}}$ and $I_{\mathrm{Tip-out}}$ are the Raman signal intensities of the tip approached to and retracted from the sample, respectively. Using the signal of the Raman peak centered at 1640 cm^{-1}, a linear enhancement of 1.6 has been measured. This number does not take into consideration the large difference between the volume probed in the FF (traditional confocal Raman microscopy) and the volume probed in the NF (TERS). Hence, a more

accurate way to quantify the signal enhancement while performing TERS is to measure EF using the following equation:

$$\mathrm{EF} = \frac{\left(I_{\mathrm{Tip-in}} - I_{\mathrm{Tip-out}}\right)}{I_{\mathrm{Tip-out}}} \cdot \frac{V_{\mathrm{FF}}}{V_{\mathrm{NF}}} \tag{1}$$

where V_{FF} and V_{NF} are the volumes probed in FF and NF, respectively [39]. Since the Rayleigh length of the focused beam is larger than the sample thickness (particularly in the flatter section of the sample where the measurement of figure 3 was executed), V_{FF} can be approximated as the volume of a cylinder with the diameter equal to the diameter of the focal spot ($2\omega_0 = 1.22 \cdot \lambda/\mathrm{NA}$) and with the height equal to the microstructure thickness (~500 nm, figure 1(c)). In the case of V_{NF}, the probed volume can instead be approximated as the volume of a cylinder having both its diameter and height equal to the metallic tip radius of curvature (~30 nm). By substituting these numbers in equation (1), a value of 10^4 is obtained for the EF of the TERS signal in figure 3. Although this number is primarily associated with the large ratio $V_{\mathrm{FF}}/V_{\mathrm{NF}}$, the measured EF is encouraging for its application in TERS characterization of TPP-DLW since it signifies that an area spanning several $\mu\mathrm{m}^2$ can be mapped in a reasonable amount of time.

The total scattered intensity in the far field reads as

$$I_{\mathrm{tot}} = I_{\mathrm{FF}} + I_{\mathrm{NF}}, \tag{2}$$

here I_{FF} and I_{NF} are the FF and NF intensities that are defined by the following relationships:

$$I_{\mathrm{FF}}(\nu) \sim \left|\mathbf{e}_s^T \overleftrightarrow{R}_\nu \mathbf{e}_e\right|^2 \tag{3a}$$

and

$$I_{\mathrm{NF}}(\nu) \sim \left|\mathbf{e}_s^T \overleftrightarrow{R}_\nu^* \mathbf{e}_e\right|^2, \tag{3b}$$

where $\overleftrightarrow{R}_\nu$ and $\overleftrightarrow{R}_\nu^*$ are Raman tensors of a vibrational mode ν without and with the tip, e_e and e_s are polarization vectors of the exciting (incident) and scattered electric fields, and the symbol $(\,)^T$ stands for the transpose [40]. In equation (2), both contributions are assumed to be incoherent. Unlike the FF intensity I_{FF}, the NF counterpart and I_{NF} contains information on mixed higher spatial frequencies of the molecule and the tip. It means that the NF image of a point source, recorded on a distant detector, is inevitably distorted by the tip, resulting in a tip-dressed optical image. The modified tensor $\overleftrightarrow{R}_\nu^*$ is defined as

$$\overleftrightarrow{R}_\nu^* = \overleftrightarrow{A}^T \overleftrightarrow{R}_\nu \overleftrightarrow{A}, \tag{4}$$

where $\overleftrightarrow{A}$ is a tip-amplification tensor [40]. In the simplest case of a cone-shaped plasmonic tip, oriented towards the z-axis (the upright position), the structure of $\overleftrightarrow{A}$ has the following form:

$$\overleftrightarrow{A} = \begin{bmatrix} a & 0 & 0 \\ 0 & a & 0 \\ 0 & 0 & b \end{bmatrix}, \tag{5}$$

where a and b are transverse and longitudinal components that are subject to the inequality $a << b$. The anisotropic structure of the tensor $\overleftrightarrow{A}$ makes the tip sensitive to the incident light polarization. In the case of the tilted tip, the tip tensor, equation (5), is generally multiplied by the rotation matrix. It is important to notice that the net EF depends not only on the tip tensor and its orientation in respect to the polymeric molecule, equation (5), but its Raman tensor as well. Since the specimen of interest represents an amorphous solid containing highly disordered polymeric chains the TERS signal noticeably fluctuates between locations. Moreover, a large difference in heights between the pad and the lines makes the TERS measurements difficult, especially when scanning over large areas. For this purpose, the TERS technique equipped with a hybrid (jumping) mode can be utilized [41].

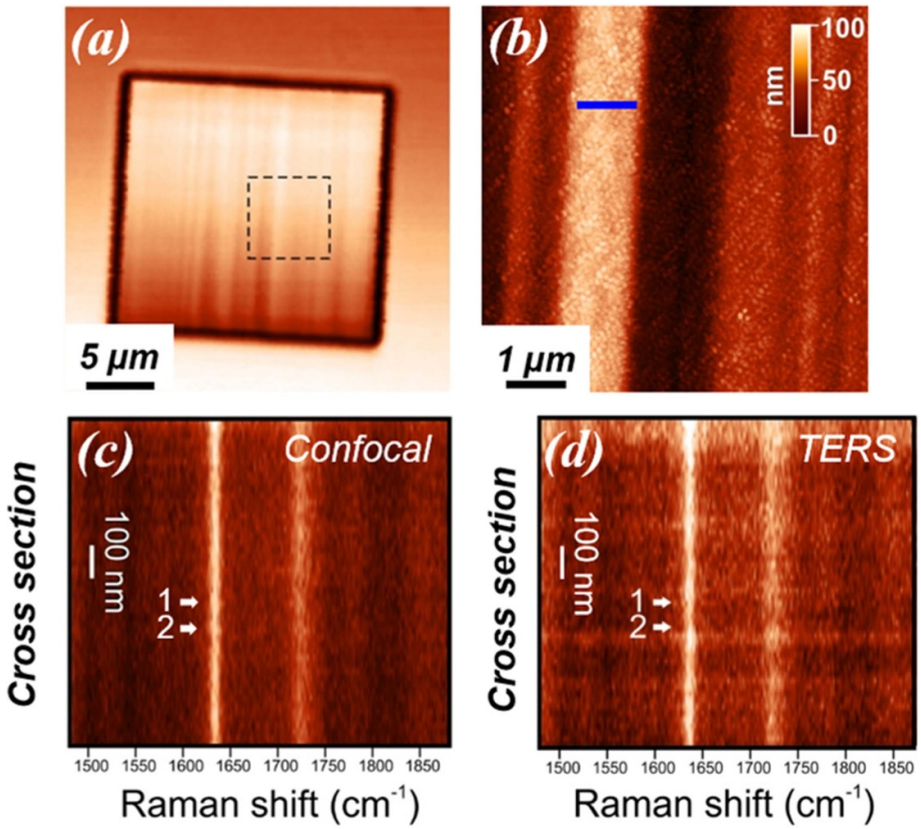

Figure 4. (a) Confocal laser image (Rayleigh scattering) of the TPP microstructure used to study TERS spatial resolution. (b) AFM image of the area of the microstructure delineated by the dashed square outline in (a). Confocal Raman microscopy and TERS 1D maps along the blue line depicted in (b) are shown in (c) and (d), respectively. The *y*-axis in the latter images represents the length of the bule line which is 1 μm. The numbers 1 and 2 in (d) designate two locations separated by a distance of 100 nm. The spectroscopic information (confocal and TERS) at these two locations is used in the next figure.

3.3. TERS vs confocal Raman microscopy spatial resolution

The TPP sample used for studying the spatial resolution in TERS consisted of a square microstructure with a side length of 20 μm. The specimen was printed by raster scanning the piezo stages assembly. The average laser power and the writing speed were 12.5 mW and 150 μm s^{-1}, respectively. The hd in the raster scan pattern was 50 nm and only one layer was written at the interface between the glass substrate and the liquid resin. A confocal laser image of this microstructure using Rayleigh scattering is shown in figure 4(a). The noticeable striation pattern of the microstructure visible in this image is most probably caused by the relatively large exposure dose and the high densities of lines used in the raster scan. This is better highlighted in figure 4(b), where a 5×5 μm^2 area of the microstructure is imaged by AFM. Features with height differences larger than 50 nm are indeed distinctly visible.

Subsequently, two 1D maps of the sample were recorded along the length of the blue line shown in figure 4(b). The corresponding FF (confocal Raman) and the NF (TERS) images are shown in figures 4(c) and (d), respectively. In these graphs, the *x*-axis plots the Raman shifts between 1500 cm^{-1} and 1800 cm^{-1} while the *y*-axis plots the length of the section of the sample investigated, which in this case spans a distance of 1 μm. Therefore, the two bright vertical lines centered at around 1640 cm^{-1} and 1720 cm^{-1} are the distribution of the alkene and carbonyl moieties within the TPP microstructure in the region of the sample defined by this line. 1D FF and NF Raman maps, shown in figures 4(c) and (d), were registered along the cross-section marked with a blue bar of 1 μm in length in figure 4(b) with a scanning step of 5 nm. The exposure time per a pixel was 1 s and, therefore, the total time to scan the TPP sample, using 5.4 mW at 532 nm as excitation, across the line in figure 4(b) was approximately 200 s.

The Raman spectra recorded in two places along this line are shown in figures 5(a) and (b). The two positions where the data is originating from are separated by only 100 nm. Their location is indicated by the number 1 and 2 in figures 4(c) and (d). The spectra collected in FF are displayed in figure 5(a), while the spectra collected in NF are displayed in figure 5(b). The distance between the two points is smaller than the spatial resolution of the optical system used in this study ($\lambda_{ex} = 532$ nm, NA $= 0.7$). Note that the spectra recorded at these two locations cannot be detected if the signal is averaged over a larger area that includes

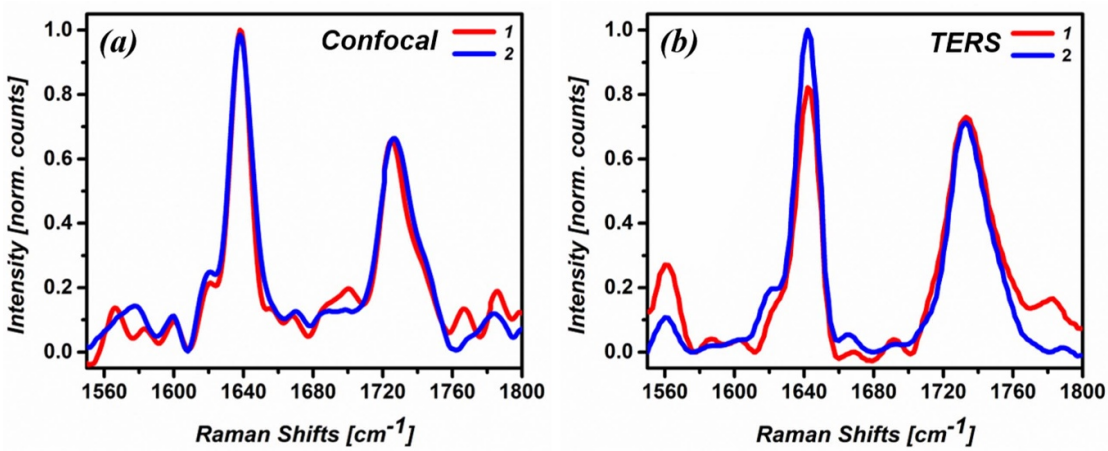

Figure 5. (a) Raman spectra of the TPP microstructure from locations 1 and 2 extracted from the confocal Raman 1D map (figure 4(c)). (b) Raman spectra of the TPP microstructure from locations 1 and 2 extracted from the TERS 1D map (figure 4(d)).

both points 1 and 2. Hence, these features cannot be discriminated in FF Raman microscopy. Indeed, we observe that the confocal Raman spectrum from point 1 is almost indistinguishable from the confocal Raman spectrum from point 2 (figure 5(a)). Specifically, the ratios between $A_{C=C}$ and $A_{C=O}$ are the same in both locations. The probing volume delivered by confocal Raman microscopy is not capable of resolving potential differences between these two points and therefore, it measures a homogenous polymer (from a DC point of view) for this part of the TPP microstructure.

A different situation is instead observed when performing TERS. From an intensity point of view indeed, the NF Raman spectrum of point 1 is different from the NF spectrum of point 2 (figure 5(b)). While $A_{C=O}$ is almost identical in the two spectra, $A_{C=C}$ in the spectrum of point 2 is appreciably larger than $A_{C=C}$ in the spectrum of point 1. From this observation, it follows that the concentration of alkene oscillators in point 2 is larger than in point 1, which can be attributed to a higher degree of polymerization in 1 than in 2. This conclusion is quantifiable by deriving the DCs of these two locations using the spectra of figure 5(b). The DC values of points 1 and 2 using TERS are 55% and 35%, respectively.

The magnitude of the TERS signal is highly dependent on the distance between the metallic tip apex and the sample surface. Thus, it is of the uttermost importance to maintain this distance constant when comparing TERS signals. In our case, the height profile of the 1 μm long section of the sample (blue line in figure 4(b)) where the FF and NF 1D maps were collected shows an overall change in height of less than 20 nm. More importantly, point 1 and point 2 in this line differ in height by less than 6 nm. These numbers are quite small and fall well within the ability of the scanning probe station employed in this study for maintaining the tip-sample separation constant though feedback.

The result presented in figure 5 is consistent with the knowledge that the structure of polymer networks obtained by the copolymerization of multifunctional monomers are quite heterogeneous at the nanoscale level [42]. Specifically, it has been demonstrated that free radical polymerization of this type of monomer produces networks with a varied distribution in space of oligomeric clusters with dimensions that range from 10 nm to 100 nm. Particularly relevant to our study is the work by Ito and coworkers where fluorescence-based NSOM was used to map the surface structure of PMMA films [43]. By labeling the monomers with fluorescent dyes, the authors of this work were able to image differences in the polymer cross-linking densities at sub-micron resolution.

Although a full understanding of the mechanisms that underlie the formation of these local cross-linked domains is lacking, it is well understood that among the factors that influence their concentration and distribution, the initial amount of cross-linker plays a dominant role. If one considers the fact that resins used in TPP-DLW are made exclusively (except for a few wt% of photoinitiator) of cross-linkers (i.e. multifunctional or branched monomers), then, the resulting polymer of the printed microstructures should inevitably contains these nano-clusters. Therefore, the $\geqslant$30% difference we observe between cross-linking at point 1 and point 2 is most likely a consequence of the structural heterogeneity formed in the polymer when performing TPP-DLW. Until now, the evidence for the nano-structure heterogeneity of cross-linked polymers formed by radical polymerization was extracted from processes that occurred in organic solvents. Hence, the result presented in figure 5 is not only the first observation of nano-structure heterogeneity of a TPP microstructure, but it is also the first direct evidence that such a phenomenon might occur in materials synthesized through bulk polymerization of resins.

These heterogeneities have important consequences for the mechanical properties of nano/microstructures fabricated by TPP, particularly when the nominal printed feature sizes are at or near the domain size of these nano-clusters. It is well documented that the DC strongly correlates with the yield strength and elastic moduli of the polymer and is routinely used as a proxy for mechanical properties [37]. In the case of the single voxel pad, the structure seems to more closely resemble an anisotropic composite than an isotropic sheet, a consequence of the laser writing direction and hatching distance. Under loading, these heterogeneities can lead to wrinkling/buckling effects which might critically affect performance. Likewise, disparities in swelling, wherein regions of lower DC absorb more solvent, could also induce premature localized failure if only the 'average DC' measured from confocal Raman microscopy is considered for material design. Finally, we notice that local differences in DC of the polymer remain engrained in the material even after pyrolysis, thus affecting the mechanical properties of ceramic nanostructures. Given the attention that ultra-strong ceramic nano-architected materials have received in the past few years [44, 45], the TERS-based technique described here provides a unique approach to probe mechanical properties and local failure mechanisms in this new exciting class of materials at an unprecedented scale.

4. Conclusions

This work demonstrates TERS characterization of polymeric microstructures fabricated by TPP-DLW. Due to the specific characteristics of TPP-DLW, we found that the optimal TERS configuration for investigating TPP microstructures is one that utilizes top illumination with a long working distance objective and a bent metallic tip. An impressive 10^4 EF was measured on microstructures printed from acrylic-based resin. Furthermore, the spatial resolution superiority of TERS versus that of confocal Raman microscopy was demonstrated by recording Raman spectra in locations within the sample that were separated by a distance of 100 nm. The TERS measurement confirmed experimentally that the structure of polymers created by TPP-DLW is heterogeneous. Specifically, the polymer network of these systems presents a distribution of nano-domains with varying cross-linking densities. With the demonstration of the feasibility of using TERS on TPP microstructures, we believe that several aspects of TPP-DLW can now be investigated with nanometric spatial resolution.

Acknowledgments

T B, L V, E G, and E P acknowledge financial support from the NSF under Grant No. CMMI-1905582. A K, E C, and S K acknowledge financial support from the Russian Science Foundation under Grant No. 19-12-00066. Scanning electron microscopy images were taken at the UCI Materials Research Institute.

ORCID iD

Tommaso Baldacchini https://orcid.org/0000-0001-9246-1653

References

[1] Maruo S, Nakamura O and Kawata S 1997 Three-dimensional microfabrication with two-photon-absorbed photopolymerization *Opt. Lett.* **22** 132
[2] Baldacchini T (ed) 2016 *Three-Dimensional Microfabrication Using Two-Photon Polymerization: Fundamentals, Technology, and Applications* (Oxford: William Andrew)
[3] Stampfl J, Liska R and Ovsianikov A (ed) 2016 *Multiphoton Lithography: Techniques, Materials, and Applications* (Weinheim: Wiley-VCH)
[4] Spiegel C S, Hippler M, Munchinger A, Bastmeywe M, Barner-Kowollik C, Wegener M and Blasco E 2020 4D printing at the microscale *Adv. Funct. Mater.* **30** 1907615
[5] Maruo S and Fourkas J T 2008 Recent progress in multiphoton microfabrication *Laser Photonics Rev.* **2** 110
[6] Malinauskas M, Farsari M, Piskarskas A and Juodkazis S 2013 Ultrafast laser nanostructuring of photopolymers: a decade of advances *Phys. Rep.* **533** 1
[7] Fischer J and Wegener M 2013 Three-dimensional optical laser lithography beyond the diffraction limit *Laser Photonics Rev.* **7** 22
[8] Juodkazis S, Mizeikis V, Seet K K, Miwa M and Misawa H 2005 Two-photon lithography of nanorods in Su-8 photoresist *Nanotechnology* **16** 846
[9] Fischer J and Wegener M 2011 Three-dimensional direct laser writing inspired by stimulated-emission-depletion microscopy *Opt. Mater. Express* **1** 614
[10] Li L, Gattass R R, Gershgoren E and Fourkas J T 2009 Achieving λ/20 resolution by one-color initiation and deactivation of polymerization *Science* **324** 910
[11] Fischer J, von Freymann G and Wegener M 2010 The materials challenge in diffraction-unlimited direct-laser-writing optical lithography *Adv. Mater.* **22** 3578
[12] Wollhofen R, Katzmann J, Hrelescu C, Jacak J and Klar T A 2013 120 nm resolution and 55 nm structure size in STED-lithography *Opt. Express* **21** 10831

[13] Gan Z, Cao Y, Evans R A and Gu M 2013 Three-dimensional deep sub-diffraction optical beam lithography with 9 nm feature size *Nat. Commun.* **4** 1
[14] Sakellari I, Kabouraki E, Gray D, Purlys V, Fotakis C, Pikulin A, Bityurin N, Vamvakaki M and Farsari M 2011 Diffusion-assisted high-resolution direct femtosecond laser writing *ACS Nano* **6** 2302
[15] Sharma R, Singh M and Sharma R 2020 Recent advances in STED and RESOLFT super-resolution imaging techniques *Spectrochim. Acta* A **231** 117715
[16] Jiang L J, Zhou Y S, Xiong W, Gao Y, Huang X, Jiang L, Baldacchini T, Silvain J-F and Lu Y F 2014 Two-photon polymerization: investigation of chemical and mechanical properties of resins using Raman microspectroscopy *Opt. Lett.* **39** 3034
[17] Pettinger B, Schambach P, Villagomez C J and Scott N 2012 Tip-enhanced Raman spectroscopy: near fields acting on a few molecules *Annu. Rev. Phys. Chem.* **63** 379
[18] Verma P 2017 Tip-enhanced Raman spectroscopy: technique and recent advances *Chem. Rev.* **117** 6447
[19] Kumar N, Mignuzzi S, Su W and Roy D, 2015 Tip-enhanced Raman spectroscopy: principles and applications *EPJ Tech. Instrum.* **2** 9
[20] Taguchi A, Yu J, Verma P and Kawata S 2015 Optical antennas multiple plasmonic nanoparticles for tip-enhanced Raman microscopy *Nanoscale* **7** 17424
[21] Yano T, Ichimura T, Kuwahara S, H'dhili F, Uetsuki K, Okuno Y, Verma P and Kawata S 2013 Tip-enhanced nano-Raman analytical imaging of locally induced strain distribution in carbon nanotubes *Nat. Commun.* **4** 2592
[22] Kumar N, Stephanidis B, Zenobi R, Wain A J and Roy D 2015 Nanoscale mapping of catalytic activity using tip-enhanced Raman spectroscopy *Nanoscale* **7** 7133
[23] Krebs F C and Norman K 2007 Analysis of the failure mechanism for a stable organic photovoltaic during 10000 h of testing *Prog. Photovolt., Res. Appl.* **15** 697
[24] Lee N, Hartschuh R D, Mehtani D, Kisliuk A, Maguire J, Green M, Foster M D and Sokolov A P 2007 High contrast scanning nano-Raman spectroscopy of silicon *J. Raman Spectrosc.* **38** 789
[25] Neugebauer U, Rosch P, Schmitt M, Popp J, Julien C, Rasmussen A, Budich C and Deckert V 2006 On the way to nanometer-sized information of the bacterial surface by tip-enhanced Raman spectroscopy *Chem. Phys. Chem.* **7** 1428
[26] Cialla D, Deckert-Gaudug T, Buddich C, Laue M, Moller R, Naumann D, Deckert V and Popp J 2009 Raman to the limit: tip enhanced Raman spectroscopy investigations of a single tobacco mosaic virus *J. Raman Spectrosc.* **40** 240
[27] Wood B R, Bailo E, Khiavi M A, Tilley L, Deed S, Deckert-Gaudug T, McNaughton D and Tip-enhanced D V 2011 Raman scattering from hemozoin crystals within a sectioned erythrocyte *Nano Lett.* **11** 1868
[28] Bailo E and Deckert V 2008 Tip-enhanced Raman spectroscopy of single RNA strands: towards a novel direct-sequencing method *Angew. Chem., Int. Ed.* **47** 1658
[29] Boon-Siang Y, Amstad E, Schmid T, Stadler J and Zenobi R 2009 Nanoscale probing of a polymer-blend thin film with tip-enhanced Raman spectroscopy *Small* **5** 952
[30] Xue L, Li W, Hoffmann G G, Goossens J G P, Loos J and de With G 2011 High-resolution chemical identification of polymer blend thin films using tip-enhanced Raman imaging *Macromolecules* **44** 2852
[31] Ober C K 2020 Materials systems for 2-photon lithography *Three-Dimensional Microfabrication Using Two-Photon Polymerization* 2nd edn, ed T Baldacchini (Oxford: William Andrew) pp 143–74
[32] Kharintsev S S, Rogov A M and Kazarian S G 2013 Nanopatterning an tuning of optical taper antenna apex for tip-enhanced Raman scattering performance *Rev. Sci. Instrum.* **84** 093106
[33] Kharintsev S, Alekseev A, Valsilchenko V, Kharitonov A and Salakhov M 2015 Electrochemical design of plasmonic nanoantennas for tip-enhanced optical spectroscopy and imaging performance *Opt. Mater. Express* **5** 2225
[34] Kharintsev S S, Noskov A I, Hoffman G G and Loos J 2011 Near-field optical taper antennas fabricated with a highly replicable ac electrochemical etching method *Nanotechnology* **22** 025202
[35] Kharintsev S S, Hoffmann G G, Dorozhkin P S, de With G and Loos J 2007 Atomic force and shear force-based tip-enhanced Raman spectroscopy and imaging *Nanotechnology* **18** 315502
[36] Baldacchini T, Zimmerley M, Potma E O and Zadoyan R 2009 Characterization of microstructures fabricated by two-photon polymerization using coherent anti-Stokes Raman scattering microscopy *J. Phys. Chem.* B **113** 12663
[37] Bauer J, Izard A G, Zhang Y, Baldacchini T and Valdevit L 2019 Programmable mechanical properties of two-photon polymerized materials: from nanowires to bulk *Adv. Mater. Technol.* **4** 1900146
[38] Žukauskas A, Matulaitiene L, Paipulas D, Niaura G, Malinauskas M and Gadonas R 2015 Tuning the refractive index in 3D direct laser writing lithography: towards GRIN microoptics *Laser Photonics Rev.* **9** 706
[39] Kumar N, Rae A and Roy D 2014 Accurate measurement of enhancement factor in tip-enhanced Raman spectroscopy through elimination of far-field artefacts *Appl. Phys. Lett.* **104** 123106
[40] Ossikovski R, Nguyen Q and Picardi G 2007 Simple model for the polarization effect in tip-enhanced Raman spectroscopy *Phys. Rev.* B **75** 045412
[41] Liu Z *et al* 2011 Revealing the molecular structure of single-molecule junctions in different conductance states by fishing-mode tip-enhanced Raman spectroscopy *Nat. Commun.* **2** 305
[42] Di Lorenzo F and Seiffert S 2015 Nanostructural heterogeneity in polymer networks and gels *Polym. Chem.* **6** 5515
[43] Aoki H, Tanaka S, Ito S and Yamamoto M 2000 Nanometric inhomogeneity of polymer network investigated by scanning near-field optical microscopy *Macromolecules* **33** 9650
[44] Bauer J, Meza L R, Schaedler T A, Schwaiger R, Zheng X and Valdevit L 2017 Nanolattices: an emerging class of mechanical metamaterials *Adv. Mater.* **29** 1701850
[45] Izard A G, Bauer J, Crook C, Turlo V and Valdevit L 2019 Ultrahigh energy absorption multifunctional spinodal nanoarchitectures *Small* **15** 1903834